49th AIAA Aerospace Sciences Meeting including the New Horizons Forum and Aerospace Exposition
4 - 7 January 2011, Orlando, Florida

AIAA 2011-412

Effects of Pressure and Gravity in Laminar Coflow Ethylene Diffusion Flames

Marc R.J. Charest*, Clinton P.T. Groth† and Ömer L. Gülder‡

University of Toronto Institute for Aerospace Studies

4925 Dufferin Street, Toronto, Ontario, M3H 5T6, Canada

The effects of pressure and gravity on sooting characteristics and flame structure were studied numerically in coflow ethylene-air laminar diffusion flames between 0.5 and 5 atm. Computations were performed by solving the unmodified and fully-coupled equations governing reactive, compressible, gaseous mixtures which include complex chemistry, detailed radiation heat transfer, and soot formation/oxidation. Soot formation/oxidation was modelled using an acetylene-based, semi-empirical model which has been verified with previously published experimental data to capture correctly many of the observed trends at normal-gravity. Calculations for each pressure considered were performed for both normal- and zero-gravity conditions to help separate the effects of pressure and buoyancy on soot formation. Based on the numerical predictions, pressure and gravity were observed to significantly influence the flames through their effects on buoyancy and reaction rates. The zero-gravity flames have higher soot concentrations, lower temperatures and broader soot-containing zones than normal-gravity flames at the same pressure. The zero-gravity flames were also found to be longer and wider. Differences were observed between the two levels of gravity when pressure was increased. The zero-gravity flames displayed a stronger dependence of the maximum soot yield on pressure from 0.5 to 2 atm and a weaker dependence from 2 to 5 atm as compared to the normal-gravity flames. In addition, flame diameter decreased with increasing pressure under normal gravity while it increased with pressure in the zero-gravity cases. Changing the prescribed wall boundary condition from fixed-temperature to adiabatic significantly altered the numerical predictions at 5 atm. When the walls were assumed to be adiabatic, peak soot volume fractions and temperatures increased in both the zero- and normal-gravity flames, emphasizing the importance of heat conduction to the burner rim on flame structure.

I. Introduction

Soot formation and oxidation strongly affects the structure and stability of laminar diffusion flames by enhancing radiation transport and altering local temperatures. Reaction rates are highly dependent upon temperature and therefore local gaseous species concentrations are strongly influenced by the presence of soot. Since the total soot yield is drastically enhanced under high-pressure [1,2] and zero-gravity conditions [3], fully understanding the soot formation process in laminar diffusion flames is essential for a variety of engineering needs. These needs range from the design of soot-free, high-pressure combustors to the development of fire-suppression systems for space applications.

Elevated pressure and zero gravity represent opposite limits of the effects of buoyancy on the structure of laminar diffusion flames. Increasing pressure under normal-gravity conditions increases chemical reaction rates and causes the expanding hot gases to accelerate more rapidly, enhancing the transport of fresh oxidizer to the reaction zone. As a result, the reaction zone narrows and the flame diameter decreases considerably as pressure is increased [1,2,4,5]. Miller and Maahs [1] suggested that this change in flame diameter with pressure is likely due to changes in chemistry. Based on a theoretical analysis, Glassman [6] concluded that the diameter of a laminar diffusion flame is proportional to $p^{-1/4}$ where p is the pressure. However, experimental measurements [4,5,7,8] and numerical predictions [9] for soot volume fraction indicate that the flame diameter is in fact proportional to $p^{-1/2}$. These findings imply that residence time is independent of pressure for constant fuel mass flow rates since the cross-sectional area of the flame varies inversely with pressure. This was confirmed numerically by Liu et al. [9] who showed that the axial velocity along the flame centerline was pressure independent. Although flame diameter decreases with increasing pressure, Roper's correlations for buoyancy-dominated laminar jet diffusion flames [10,11] state that the visible flame height, to a first-order

*PhD Candidate, Email: charest@utias.utoronto.ca, Student Member AIAA
†Professor, Email: groth@utias.utoronto.ca, Senior Member AIAA
‡Professor, Email: ogulder@utias.utoronto.ca, Associate Fellow AIAA

approximation, is independent of pressure and depends on mass flow rate only. However, Miller and Maahs [1], Flower and Bowman [2], McCrain and Roberts [4], and Thomson et al. [5] have all observed pressure-dependent flame heights during experiments involving high-pressure laminar diffusion flames. These experiments generally showed that the visible flame height initially increased with pressure at low pressures, remained constant over a range of pressures, and then decreased with further increase in pressure. Recently, pressure-independent visible flame heights were observed over a wide range of pressures by Bento et al. [7] and Joo and Gülder [8]. Constant flame heights with increasing pressure were also predicted numerically by Liu et al. [9] and Charest et al. [12].

Buoyancy forces are completely eliminated in zero-gravity environments. Local flow velocities in the flame are significantly reduced and the transport of fresh reactants to the reaction zone is slowed. As a result, non-buoyant flames are longer and wider than their buoyant counterparts [13–16]. Sunderland et al. [16] observed the shapes of non-buoyant and buoyant flames and found that stoichiometric flame lengths were proportional to fuel mass flow rate only, independent of pressure and burner diameter. The shapes of non-buoyant flames were also demonstrated to approach those of buoyant ones as jet Reynolds numbers are increased.

In both limiting cases, high-pressure and zero-gravity, soot formation is significantly enhanced [6]. As pressure is increased in normal-gravity flames, measured soot volume fractions increase since the flame narrows and soot must flow through a smaller cross-section. This narrowing of the flame causes local temperatures near the centerline to increase and fuel pyrolysis rates in the central core to intensify. Enhanced air entrainment into the flame near the burner is also expected to increase pyrolysis rates [9]. In addition to an increase in soot volume fractions with pressure, there is an increase in the amount of fuel carbon which is converted to soot. Miller and Maahs [1] estimated total soot concentrations in high-pressure axisymmetric methane-air diffusion flames between 1 to 50 atm based on measurements of flame emissive power. The data indicates that soot yield is proportional to p^n, where n is approximately 1.7±0.7 up to 10 atm. Above 10 atm, the dependence of soot yield on pressure decreased significantly. Flower and Bowman [2] studied laminar diffusion flames of ethylene at pressures between 1 and 10 atm by measuring line-of-sight integrated soot volume fractions and temperatures along the flame centerline. They reported maximum diameter-integrated soot volume fractions proportional to $p^{1.2}$. Measurements made by Lee and Na [17] in laminar ethylene diffusion flames from 1 to 4 atm indicated a $p^{1.26}$ dependence of the maximum diameter-integrated soot volume fraction on pressure. McCrain and Roberts [4] obtained similar pressure exponents in methane flames from 1 to 25 atm and ethylene flames from 1 to 16 atm based on path-integrated and local soot volume fraction measurements. Radially-resolved soot concentration and temperature measurements were reported by Thomson et al. [5] for methane diffusion flames from 5 to 40 atm which were later extended to 60 atm by Joo and Gülder [8]. Both concluded that the maximum amount of fuel carbon converted to soot, which is most suitable for assessing the sensitivity of soot formation to pressure [2], varied proportional to p between 5 to 20 atm. Between 30 and 60 atm, Joo and Gülder measured a pressure exponent equal to 0.33. A large increase in radial temperature gradients near the burner exit was also measured as pressures increased. These larger temperature gradients are expected to intensify thermal diffusion from the hot regions of the flame towards the flame centerline. As a result, soot nucleation and growth is enhanced. Similar soot and temperature measurements were made by Bento et al. [7] for propane flames from 1 to 7.2 atm.

Non-buoyant diffusion flames, i.e., zero-gravity flames, exhibit broader soot-containing regions and larger soot oxidation regions [18]. Since soot particles are too large to diffuse like gas molecules, they are primarily convected by the gas flow. Their behaviour in buoyant and non-buoyant laminar diffusion flames is therefore quite different since flow streamlines are drastically altered by buoyancy [19]. For example, the dividing streamline defined by the locus of points where the radial velocity component is zero diverges radially-outward in non-buoyant jet diffusion flames and converges towards the centerline in buoyant ones. As such, soot particles follow different paths in non-buoyant and buoyant flames. In addition to altered streamlines, residence times in non-buoyant flames are much larger than in buoyant flames, resulting in higher soot concentrations and bigger particles [3,20,21]. Radiative heat losses are also enhanced and flame temperatures reduced as a result of the long residence times in non-buoyant flames.

There are many experimental studies on the sooting characteristics of non-buoyant diffusion flames [19,22]. Smoke-point measurements reported by Sunderland et al. [19] and Urban et al. [22] for various gaseous hydrocarbon fuels indicated that the laminar smoke-point flame lengths of non-buoyant flames were much shorter than equivalent buoyant flames. Ku et al. [20] measured soot particle sizes in laminar diffusion flames of propane and ethylene under normal- and micro-gravity conditions. They found that primary particle sizes were larger in non-buoyant flames due to the longer residence times. Soot volume fractions were measured and soot particles sampled in weakly-buoyant gaseous laminar diffusion flames at sub-atmospheric pressures by Sunderland et al. [23–25]. These authors exploited the fact that the buoyancy-induced acceleration scales with p^2g where g is the gravitational acceleration. Others have obtained quantitative two-dimensional measurements for soot volume fraction in either reduced-gravity [3,21,26–28] or zero-gravity [29–31] environments. Generally, measured peak soot concentrations in micro-gravity flames are approximately a factor of

two larger than those measured in normal-gravity flames.

Numerical modeling is an attractive tool to study the effect of pressure and gravity on soot formation in gaseous laminar diffusion flames. Measurements in high-pressure laminar diffusion flames are complicated by small flame diameters and limited optical access[9] while it is difficult and costly to conduct zero-gravity experiments[32]. Drop-towers do not provide sufficient time to reach steady-states and experiments on parabolic flights are subjected to small fluctuations in gravity, called g-jitter. Experiments aboard spacecraft in orbit can provide long, zero-gravity environments, but such experiments are limited by high costs and payload size/weight. Alternatively, buoyancy can be minimized by reducing pressure below atmospheric. However, low-pressure experiments are not representative of true, zero-gravity flames as flames are not completely isolated from the effects of gravity and reactions rates are slow[33].

There are only a few numerical studies of the effects of gravity[18,34–37] and pressure[9,12,38] on soot formation in gaseous laminar diffusion flames. The detailed numerical study by Liu et al.[9] on methane-air diffusion flames at pressures between 5 and 40 atm showed large discrepancies between measurements and predictions. These discrepancies are primarily due to the inability of simplified soot formation/destruction models to accurately predict soot concentrations. Similar quantitative results were obtained by Charest et al.[12] for detailed numerical studies of high-pressure ethylene-air flames. These studies showed that the effect of pressure on global quantities such as the carbon conversion factor were well-captured by a simple, acetylene-based soot model[39,40]. Since two-dimensional, spatially-resolved measurements for soot volume fraction and temperature have only recently been published[31], soot formation models have not been validated for zero-gravity flames.

There is only one detailed numerical study of soot formation in zero-gravity gaseous laminar diffusion flames[36]. This particular study investigated the effects of gravity and coflow velocity on the structure and soot yield of methane-air laminar diffusion flames. In the study, reducing gravity was observed to cause local extinction and suppress soot formation when coflow velocities were below a critical level. Walsh et al.[28] numerically studied the effect of buoyancy on the temperature and species concentrations in lifted laminar diffusion flames. However, these flames were weakly-sooting and soot was not accounted for in the model.

Recently, Panek and Gülder[33] obtained detailed line-of-sight measurements for soot volume fraction and temperature in laminar diffusion flames of ethylene at sub- and super-atmospheric pressures. They found that the measurements for soot volume fraction in the weakly-buoyant flames were not consistent with the results recorded in drop towers, parabolic flights, and spacecraft. Rather, the results followed trends consistent with high-pressure experiments since less soot was formed in the weakly-buoyant, sub-atmospheric flames than in the buoyant, atmospheric-pressure flame.

The goal of the present research is to numerically study the effects of buoyancy and pressure on the structure of laminar diffusion flames. As a starting point, the weakly-buoyant flames studied by Panek and Gülder[33] were modelled and the predictive accuracy of the numerical model was verified. The numerical results were also used to explain some of the experimental observations. A second set of calculations were performed neglecting gravity to separate and identify more clearly the effects of buoyancy and pressure on soot formation. This paper first presents a brief overview of the numerical model and the coflow burner configuration. Following this overview, the results are discussed and the conclusions presented.

II. Numerical Model

The present study makes use of a previously developed framework for modelling laminar reactive flows with complex chemistry, non-gray radiative heat transfer and soot[41]. This framework mathematically describes the gaseous combusting flow using the conservation equations for continuous, multi-component compressible gas mixtures[42]. The equations consist of the conservation of total mass, individual species mass, mixture momentum, and mixture energy. Soot formation and destruction is modelled using an approach similar to those developed by Leung et al.[39] and Fairweather et al.[43]. In this approach, the soot particle size distribution is approximated by an average size that varies via surface reactions and coagulation. The representation requires only two additional transport equations for soot mass and number, which are given by

$$\frac{\partial}{\partial t}(\rho Y_s) + \nabla \cdot [\rho Y_s(\mathbf{v} + \mathbf{V}_Y)] = S_Y \tag{1}$$

$$\frac{\partial}{\partial t}(\rho N_s) + \nabla \cdot [\rho N_s(\mathbf{v} + \mathbf{V}_N)] = S_N \tag{2}$$

where t is the time, ρ is the mixture density, $\mathbf{v}$ is the mixture velocity vector, Y_s is the mass fraction of soot, N_s is the soot number density (number of particles per unit mass of mixture), $\mathbf{V}_Y$ is the diffusion velocity related to soot

mass, $\mathbf{V}_N$ is the diffusion velocity related to soot number, S_Y is the time rate of change of the soot mass, and S_N is the time rate of change of the soot number. The time rate of change of gaseous species includes contributions from both gas-phase chemistry and soot surface reactions. The density of the mixture was calculated using the following state equation:

$$\rho = \frac{p}{R_u T \left(\sum_{k=1}^{N} Y_k / M_k\right)} \tag{3}$$

where p is the mixture pressure, Y_k is the mass fraction of the kth gaseous species, N is the number of gaseous species in the mixture, R_u is the universal gas constant, T is the temperature, and M_k is the species molar mass.

Multi-species diffusion was modelled here using the first-order Hirschfelder and Curtiss approximation[44] while soot was assumed to diffuse primarily by thermophoresis using a model based on the limit of free-molecular flow[45,46]. In addition to contributions from thermophoresis, a small Fickian diffusive flux was included in the soot particle transport equations. This was required to enhance numerical stability even though the transport of soot via Brownian motion is generally negligible. A similar procedure was taken by Kennedy et al.[47]. The resulting diffusion velocities for soot are

$$\mathbf{V}_Y = -\frac{D_s}{Y_s}\nabla Y_s + \mathbf{V}_T \tag{4}$$

$$\mathbf{V}_N = -\frac{D_s}{N_s}\nabla N_s + \mathbf{V}_T \tag{5}$$

where $D_s = 10^{-8}$ m^2/s is the soot diffusion coefficient. Similarly, Kennedy et al.[47] specified a value for D_s equal to 1% of the gas diffusivity. The thermophoretic velocity, $\mathbf{V}_T$, for the soot particles is[45]

$$\mathbf{V}_T = -0.55\frac{\mu}{\rho T}\nabla T \tag{6}$$

where μ is the mixture dynamic viscosity.

A. Soot Chemistry Model

Soot formation and destruction was modelled using the simplified soot kinetics described by Liu et al.[9,40] This model is based on the reduced soot mechanisms of Leung et al.[39] and Fairweather et al.[43] which describe the evolution of soot through four basic steps—nucleation, surface growth, coagulation, and oxidation. Acetylene is assumed to be the only precursor responsible for the presence of soot. The resulting mechanism is

$$C_2H_2 \longrightarrow 2\,C(s) + H_2 \tag{7}$$

$$C_2H_2 + n{\cdot}C(s) \longrightarrow (n+2){\cdot}C(s) + H_2 \tag{8}$$

$$C(s) + \tfrac{1}{2}O_2 \longrightarrow CO \tag{9}$$

$$C(s) + OH \longrightarrow CO + H \tag{10}$$

$$C(s) + O \longrightarrow CO \tag{11}$$

$$n{\cdot}C(s) \longrightarrow C_n(s) \tag{12}$$

It follows from the mechanism above that the source term in Eq. (1) can be written as

$$S_Y = 2M_s(R_1 + R_2) - (R_3 + R_4 + R_5)A_s \tag{13}$$

where M_s is the molar mass of soot (assumed equal to the molar mass of carbon, 12 kmol/kg) and A_s is the surface area of soot per unit volume of aerosol. The terms R_3, R_4, and R_5 are the soot oxidation rates for reactions involving O_2, OH, and O, respectively. The terms R_1 and R_2 are the soot nucleation and surface growth rates defined by

$$R_1 = k_1[C_2H_2] \tag{14}$$

$$R_2 = k_2 f(A_s)[C_2H_2] \tag{15}$$

The function $f(A_s)$ incorporates the dependence of soot surface growth on the soot surface area per unit volume, A_s. Proposed forms of $f(A_s)$ include[39,43]: $f(A_s) = A_s^{0.5}$ and $f(A_s) = A_s$. Here we have used the first relationship. The corresponding rate constants, k_1 and k_2, are given by[40]

$$k_1 = 1000\exp(-16\,103/T) \tag{16}$$

$$k_2 = 1750\exp(-10\,064/T) \tag{17}$$

Surface area is related to the soot mass and number density by

$$A_s = \pi \left(\frac{6}{\pi} \frac{1}{\rho_s} \frac{Y_s}{N_s} \right)^{2/3} (\rho N_s) \tag{18}$$

where ρ_s is the density of soot, taken to be 1900 kg/m^3. The oxidation reaction rates per unit surface area are modelled by [9]

$$R_3 = 120 \left\{ \frac{k_a p_{O_2} \chi}{1 + k_z p_{O_2}} + k_b p_{O_2} (1 - \chi) \right\} \tag{19}$$

$$R_4 = \varphi_{OH} k_4 T^{-1/2} p_{OH} \tag{20}$$

$$R_5 = \varphi_O k_5 T^{-1/2} p_O \tag{21}$$

where

$$\chi = \left\{ 1 + \frac{k_T}{k_b p_{O_2}} \right\}^{-1} \tag{22}$$

The symbols p_{O_2}, p_{OH} and p_O denote the partial pressures of O_2, OH and O in atm, respectively. The collision efficiencies for OH, φ_{OH}, and O, φ_O, were both assumed equal to 0.2. The rate of soot oxidation by O_2 was based on the Nagle-Strickland-Constable model [48] with the rate constants k_a, k_b, k_z, k_T, and k_4 taken from Moss et al. [49]. The rate constant k_5 was equal to the value used by Bradley et al. [50].

The source term in Eq. (2) represents the production and destruction of the soot particle number density with nucleation and agglomeration. It is modelled herein as follows:

$$\begin{aligned} S_N = & \frac{2}{C_{min}} N_a R_1 \\ & - 2 C_a \left(\frac{6 M_s}{\pi \rho_s} \right)^{1/6} \left(\frac{6 k_B T}{\rho_s} \right) [C(s)]^{1/6} (\rho N_s)^{11/6} \end{aligned} \tag{23}$$

where N_a is Avogadro's number (6.022×10^{26} kmol^{-1}), k_B is the Boltzmann constant (1.38×10^{-23} m^2 kg s^{-2} K^{-1}), $C_{min} = 700$ is the number of carbon atoms in the incipient carbon particle, C_a is the agglomeration rate constant, and $[C(s)] = \rho Y_s / M_s$ is the molar concentration of soot. Based on the recommendations of Liu et al. [9] and Ezekoye and Zhang [34], agglomeration was neglected by setting C_a to zero.

Several issues related to numerical stability and convergence were encountered using the previously described soot model. First, both S_Y and S_N are functions of Y_s and N_s raised to sub-unity powers. For example,

$$S_Y \propto Y_s^{1/3} N_s^{1/6} \quad \text{and} \quad S_N \propto Y_s^{1/6} \tag{24}$$

As a result, derivatives of S_Y and S_N with respect to Y_s or N_s become infinite as $Y_s \to 0$ or $N_s \to 0$. Additionally, oscillations in Y_s or N_s caused by round-off and numerical diffusion errors can produce large fluctuations in the source terms when Y_s and N_s are small. Both of these issues caused the Newton-Krylov time-marching algorithm applied herein to stall. To overcome this stall, A_s was modified by applying a blending function to eliminate any on/off switching experienced by S_Y and smooth its derivative with respect to Y_s and N_s. The modified surface area is given by

$$A_s^* = \beta(Y_s) \beta(N_s) A_s \tag{25}$$

where the blending function, $\beta(x)$, is defined as

$$\beta(x) = 1.0 - \exp\left[-5 \left(\frac{x}{10^{-6}} \right)^2 \right] \tag{26}$$

The modification was applied by replacing A_s with A_s^* in Eqs. (13) and (15).

B. Radiation Model

Radiation emitted and absorbed by both the gas and soot is modelled using the discrete ordinates method (DOM) coupled with the point-implicit finite volume approach of Carlson and Lathrop [51]. Spatial derivatives are evaluated using centered differences while ordinate directions and weights were selected based on the T_3 quadrature set [52].

Spectral absorption coefficients are approximated using a wide-band model which is based on the statistical narrow-band correlated-k (SNBCK) model[53]. Four Gauss quadrature points were found to provide a reasonable balance between accuracy and computational expense when integrating the DOM equations over each band[54,55]. In this work, the narrow-band data of Soufiani and Taine[56] for H_2O, CO_2 and CO are used to construct the cumulative distribution function. To reduce the number of unknowns required for non-gray radiation in mixtures, the three radiating gases are approximated by a single gas with effective narrow-band parameters based on the optically thin limit[57]. Additional computational savings are achieved by combining bands to form several wide bands using the lumping procedure described by Liu et al.[53]. Based on the recommendations of Goutiere et al.[58], a total of nine non-uniformly spaced wide bands are employed. The spectral absorption coefficient for soot is determined based on the Rayleigh limit for small spherical particles[40].

C. Numerical Solution Procedure

The equations governing the gas-particle mixture described previously are solved numerically using a finite-volume scheme previously developed by Groth and co-workers[41,59,60]. The scheme makes use of piecewise limited linear reconstruction and an approximate Riemann solver to determine the inviscid fluxes[61]. The second-order diamond-path method developed by Coirier and Powell[62] was used to compute the viscous fluxes. Both the inviscid flux and the temporal derivative are preconditioned using the proposed matrix of Weiss and Smith[63]. This preconditioning helps reduce excessive dissipation and numerical stiffness commonly encountered when applying the compressible gas equations to low-Mach-number flows. The solution of the fully-coupled non-linear ODEs are relaxed to a steady-state using the block-based parallel implicit algorithm developed by Northrup and Groth[59] which makes use of a matrix-free inexact Newton-Krylov method. Solution of the DOM equations is decoupled from the gas-particle flow equations and solved sequentially at each time step.

Thermodynamic and transport properties along with gas-phase kinetic rates are evaluated using CANTERA[64], an open-source software package for chemically-reacting flows. The simulations were performed using the skeletal mechanism of Law[65] for ethylene-air combustion which consisted of 33 species and 205 elementary reactions. This mechanism was derived from the detailed one proposed by Qin et al.[66] through skeletal reduction whereby unimportant species and the reactions involving them are eliminated based on a sensitivity analysis.

III. Coflow Burner Configuration and Problem Formulation

The experimental apparatus used by Panek and Gülder[33] consists of a coflow burner housed inside a cylindrical pressure vessel. The burner has a central fuel tube with a 3 mm exit diameter and a concentric coflow-air tube with a 25.4 mm inner diameter. This apparatus is described in detail elsewhere[5,7,8]. Both the inner and outer surfaces of the fuel tube are chamfered with a round edge at the nozzle exit plane, which introduces uncertainties in the fuel's outlet velocity profile. A chimney was used to improve flame stability by shielding the core flow from disturbances created inside the chamber. This chimney has an inner diameter of 25.4 mm. For all the flames, constant mass flow rates for ethylene and air of 0.482 mg/s and 0.11 g/s were maintained, respectively, corresponding to an equivalent carbon flow rate of 0.412 mg/s. Panek and Gülder obtained measurements for temperature and soot volume fraction in flames at pressures between 0.5 and 5 atm, so calculations were performed at 0.5, 0.7, 1, 2 and 5 atm. While experimental measurements were only obtained under normal-gravity conditions, the calculations were performed for both normal- and zero-gravity levels. The temperature of the fuel and air supplied to the burner was assumed to be equal to 300 K for all cases.

A. Computational Domain and Boundary Conditions

The two-dimensional computational domain used for the coflow burner is shown schematically in Fig. 1 along with the applied boundary conditions. The domain extends radially outwards 20 mm and downstream 25 mm. The far-field boundary was treated using a free-slip condition which neglects any shear imparted to the coflow air by the chimney walls. The modelled domain is also extended 9 mm upstream into the fuel and air tubes to account for the effects of fuel preheating[67] and better represent the inflow velocity distribution. At the outlet, temperature, velocity, species mass fractions and soot number density are extrapolated while pressure is held fixed. The gas/soot mixture is specified at the inlet along with velocity and temperature while pressure is extrapolated. Uniform velocity and temperature profiles were specified for both the fuel and air inlet boundaries. For the radiation solver, all boundaries except for the axis of symmetry are assumed to be cold and black.

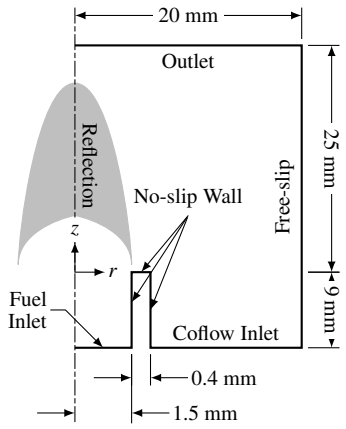

Figure 1. Computational domain and boundary conditions.

A simplified representation of the fuel tube geometry was employed to reduce the numerical complexity of this particular problem. As shown in Fig. 1, the chamfered edge of the fuel tube was approximated by a tube with 0.4 mm uniformly-thick walls. The three surfaces that lie along the tube wall were modelled as fixed-temperature walls at 300 K with zero-slip conditions on velocity.

The computational domain in Fig. 1 was subdivided into 192 cells in the radial- and 320 in the axial-direction to form a structured, non-uniformly-spaced mesh of 60 000 cells. These cells were clustered towards the burner exit plane to capture interactions near the fuel tube walls and towards the centerline to capture the core flow of the flame. A fixed mesh spacing of approximately 35 μm was specified in the radial-direction between r=0 and r=4.8 mm. The vertical spacing approaches 5.6 μm near the fuel tube exit plane. The same mesh was employed for all calculations, zero- and normal-gravity, to facilitate the comparison. Increasing the mesh resolution did not significantly improve the numerical solution.

All computations were performed on a high performance parallel cluster consisting of 104 IBM P6-575 nodes with 128 GB RAM per node and a high-speed interconnect. The nodes each have 32 IBM POWER6 cores (4.7GHz) and are connected to a non-blocking switch with four 4x-DDR InfiniBand links.

IV. Verification with Measurements

The predictions for the normal-gravity flames are first compared to the experimental measurements of Panek and Gülder [33] to assess the predictive accuracy of the numerical model. Following this assessment, the numerical results obtained for the normal- and zero-gravity flames are compared.

Predicted radial profiles for soot volume fraction and temperature are compared with the experimental measurements obtained by Panek and Gülder [33] in Fig. 2 for each operating pressure investigated. Only the numerical results obtained for the normal-gravity flames are presented in the figure. Three axial locations were chosen for this comparison: low in the flame where soot particles undergo nucleation and growth, the middle of the flame near the maximum soot volume fraction, and higher in the flame where soot is oxidized. The model predicts many of the experimentally-observed trends, but generally over-predicts soot volume fractions throughout the 0.5 to 1 atm flames and under-predicts soot in the 2 and 5 atm flames.

In both the experiments and calculations, soot is formed in an annulus downstream of the fuel tube rim. The measured soot volume fractions initially increase with height and then decrease as soot is oxidized higher up in the flame. This initial increase is not predicted between the three axial heights shown in Fig. 2 as soot volume fractions have already begun decreasing at the lowest height considered for each flame. This discrepancy suggests that the numerical model predicts the initial formation of soot lower in the flame than measured. As pressure is increased, the location of the peaks in the measured radial profiles for soot volume fraction contract radially-inwards, the peaks become more pronounced, and soot concentrations increase. While these features are observed in the numerical results, the magnitudes of the computed soot volume fractions are greatly over-predicted in most cases, especially in the annular region with high soot concentrations. The degree of this over-prediction is largest at 0.5 atm and diminishes as pressure is increased. At 5 atm, the calculations under-predict the peak soot volume fractions by about a factor of two.

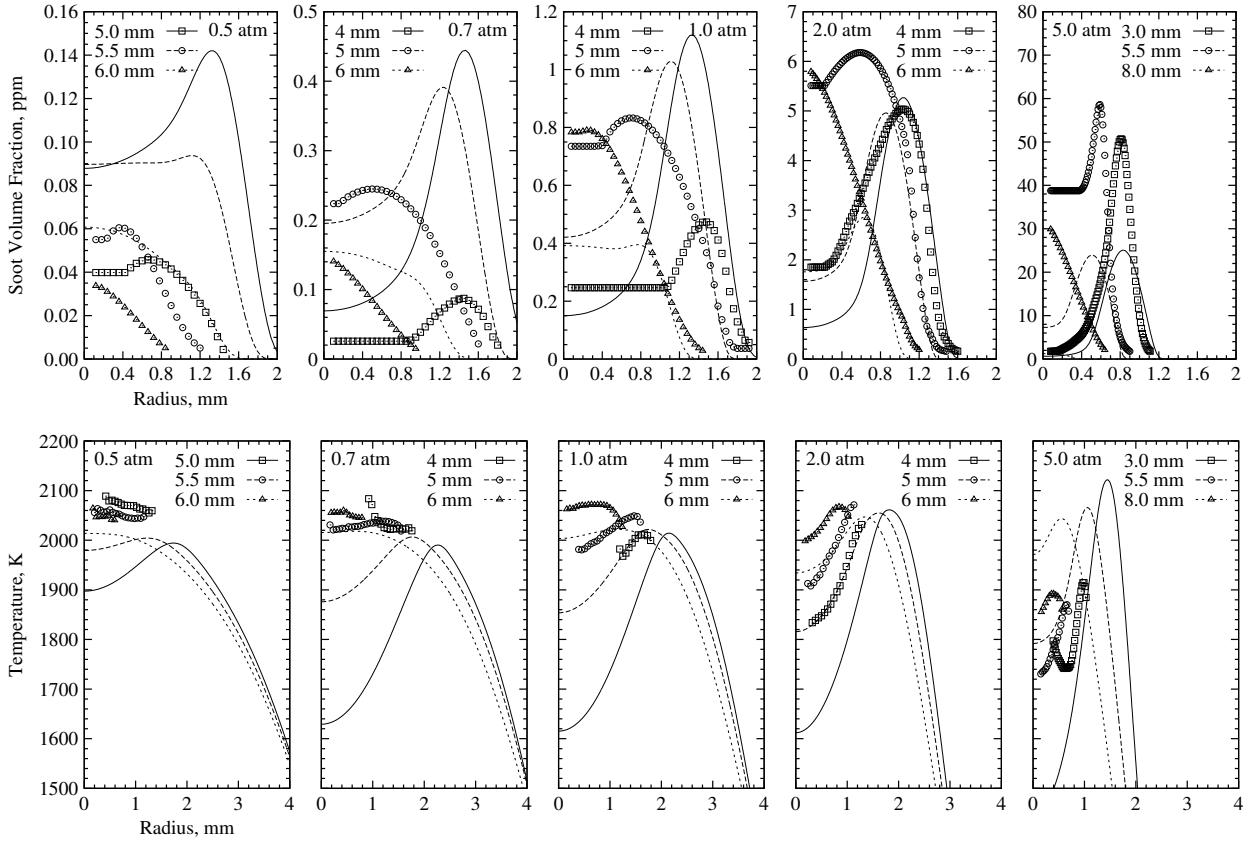

Figure 2. Measurements of Panek and Gülder [33] (symbols) and numerical predictions (lines) for radial profiles for soot volume fraction and temperature at various flame heights.

Despite the errors in the predicted soot volume fraction, the computed radial temperature profiles given in Fig. 2 agree quite well with the measurements. One exception occurs at 5 atm where peak temperatures are over-predicted by up to 200 K. Moreover, the observed discrepancies for temperature do not explain the errors in the computed soot volume fraction that were discussed previously. At low pressures, between 0.5 and 1 atm, temperatures are under-predicted while soot volume fraction is over-predicted. The opposite is observed at 5 atm. In all flames, the temperatures along the centerline are somewhat under-estimated.

Similar relationships between pressure, flame height, and temperature are observed in both the numerical predictions and experimental measurements. The experimental and numerical temperature profiles possess an annular structure similar to the radial profiles for soot volume fraction except that the radial location where temperature peaks occurs at a much larger radius. With increasing height in the flame, the location of the peak temperatures gradually shifts towards the centerline in both sets of results. A slight increase in temperature with increasing height is observed in the numerical results, except between 2 and 5 atm where peak temperatures steadily decrease with increasing height. While similar trends were also measured, the small number of valid temperature measurements makes a detailed comparison rather difficult. For example, the measured peak temperatures increase with height in the 0.7, 1, and 2 atm flames while they decrease with height in the 0.5 and 5 atm flames.

A. Soot Volume Fraction Contours

Two-dimensional contour plots of soot volume fraction were constructed from the experimental measurements and are compared with the numerical results for the normal-gravity flames in Fig. 3. Qualitatively, the predicted and measured flame geometries are similar and the narrowing of the flame with increasing pressure is clearly observed in both sets of results. The flame height based on soot volume fraction between 0.5 and 1 atm is also accurately predicted by the model. Within this range of pressures, a constant height of approximately 6.7 mm is predicted when the edge of the visible flame is approximated by the isocontour where the soot volume fraction is equal to 0.01 ppm. While

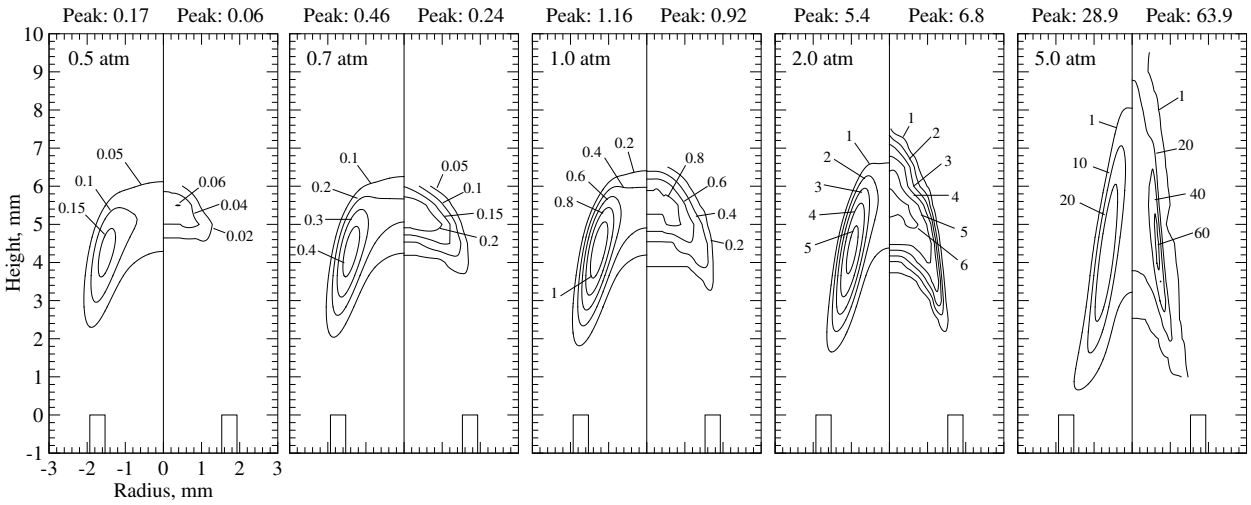

Figure 3. Predicted (left) and measured (right) contours for soot volume fraction in ppm. Experimental measurements are taken from Panek and Gülder [33].

the measured heights are comparable, it is difficult to clearly distinguish a visible flame height from the measured contours since the tip of the flame appears cut off. As pressure is increased from 1 to 5 atm, both the measured and predicted flame heights increase, but the model under-predicts this increase. A height of roughly 8.5 mm is predicted at a pressure of 5 atm compared to a measured height of 9.5 mm. The model also incorrectly predicts the location of the peak soot volume fraction and, in general, some significant differences between predicted and measured soot concentrations are observed at lower flame heights. Soot is predicted to reach a maximum in an annular region near the middle of the flame whereas the peak is experimentally-observed to occur along the centerline near the flame tip. The measurements display a more pronounced annular structure at 5 atm. Additionally, the model always predicts that soot production begins further upstream than in the experiments. With increasing pressure, both experiments and predictions show that soot formation begins lower in the flame and that the annular structure becomes thinner. However, these observations are more pronounced in the experimental measurements.

B. Soot Yield

To assess the fuel's propensity to soot and its sensitivity to pressure, the variation in the carbon conversion factor with pressure was studied. This factor is defined as $\eta_s = \dot{m}_s/\dot{m}_c$ where $\dot{m}_c$ is the carbon mass flow rate at the nozzle exit[2]. The mass flux of soot through a horizontal cross-section is

$$\dot{m}_s = 2\pi\rho_s \int f_v v r \, dr \tag{27}$$

where $\rho_s = 1.9$ g/cm^3 is the density of soot[40], f_v is the soot volume fraction and v is the axial velocity. Since the velocity is not known in the experiments, it is estimated by $v = \sqrt{2az}$ where z is the height above the burner and a is an acceleration constant commonly assumed equal to 25 m/s^2 (Ref. 11). However, at sub-atmospheric pressure, assuming non-buoyant conditions, the acceleration varies proportional to the square of pressure, $a \propto p^2$ (Ref. 32). Therefore, $a = 12.25$ m/s^2 at 0.7 atm and $a = 6.25$ m/s^2 at 0.5 atm. The computed velocity was also used as an alternative to estimate $\dot{m}_s$ in Eq. (27) using the experimentally-measured soot volume fractions.

The effect of pressure on the predicted and measured maximum η_s for the normal-gravity flames is presented in Fig. 4. Numerical results obtained using a gravitational constant of 0 m/s^2 are also provided in the figure, but they are not discussed until the following section. As observed in the figure, the normal-gravity calculations greatly over-predict the experimental values at 0.5 atm. Nonetheless, the agreement between measurements and predictions improves as pressure is increased to 2 atm. At 5 atm, the maximum amount of fuel carbon that is converted to soot is under-predicted. It is believed that the larger differences at low pressures (0.5 and 0.7 atm) are caused by systematic errors in the values for soot volume fraction derived using the spectral soot emission (SSE) diagnostic technique. SSE errors become large as soot volume fractions decrease below 0.5 to 1 ppm since measured intensities approach the background levels. This may also explain the extremely large measured dependence of η_s on pressure at low

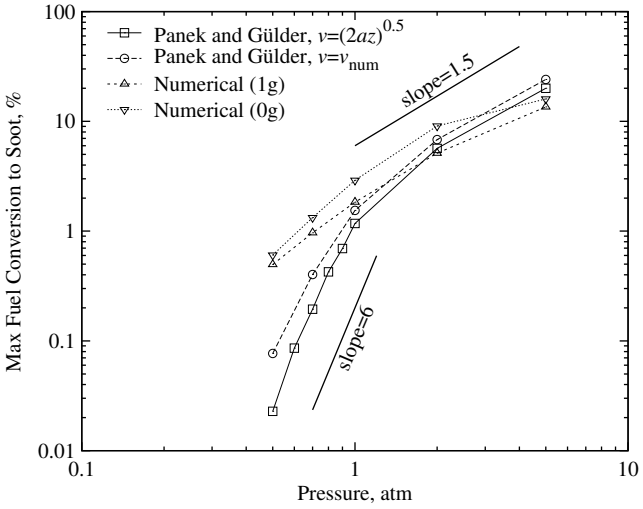

Figure 4. Maximum fuel carbon converted to soot as a function of pressure.

pressures. The measured relationship between η_s and pressure is approximately $\eta_s \propto p^{5.6}$ between 0.5 to 1 atm and $\eta_s \propto p^{1.8}$ between 1 and 5 atm (based on $v = \sqrt{2az}$). Using the calculated velocity instead of $v = \sqrt{2az}$ to determine the experimental values for η_s does not significantly affect these observed trends with pressure ($\eta_s \propto p^{4.3}$ between 0.5 to 1 atm and $\eta_s \propto p^{1.7}$ between 1 and 5 atm), but shifts the values for η_s upward slightly. Numerical predictions for the maximum η_s in the normal-gravity flames display a dependence proportional to $p^{1.7}$ between 0.5 to 2 atm and $p^{1.1}$ from 2 to 5 atm. While the model correctly predicts the decreasing sensitivity of the peak η_s with increasing pressure, the strength of this pressure dependence is always under-predicted and the magnitudes of the peak η_s are over-predicted. This under-estimated pressure-dependence is consistent with the over-predicted soot volume fractions at low pressures and under-predicted soot volume fractions at 5 atm that were observed in Figs. 2 and 3.

V. Effects of Gravity and Pressure

A. Soot Yield

As observed in Fig. 4, gravity has a large effect on the predicted maximum value for η_s. The maximum η_s at each pressure is larger in zero-gravity with the largest difference between the two, a factor of 1.7, occurring at a pressure of 2 atm. There is also a significant change in the relationship between η_s and pressure when gravity is eliminated. For example, the maximum η_s in the zero-gravity flames displays a dependence on pressure proportional to $p^{2.0}$ from 0.5 to 2 atm and $p^{0.6}$ from 2 to 5 atm. This observed zero-gravity relationship between η_s and pressure is stronger than predicted in normal-gravity at low pressures and weaker at high pressures.

The differences observed between the η_s-pressure relationships at the two levels of gravity are partially explained by comparing the local variation of the soot mass fraction along a soot particle's path, shown in Fig. 5 for each flame. In the figure, the trajectory of the soot particle originates at the reaction zone and passes through the region of maximum soot volume fraction. The reaction zone was designated by the location where the mixture fraction is stoichiometric. A similar procedure was performed by Honnery and Kent[68,69] to analyze experimental measurements in laminar diffusion flames of ethylene and ethane.

For this numerical study, the mixture fraction was computed using the following relation proposed by Bilger[70] for ethylene-air flames:

$$Z = \frac{\frac{1}{2}Y_C/M_C + \frac{1}{4}Y_H/M_H + \frac{1}{3}(Y_{O,2} - Y_O)/M_O}{\frac{1}{2}Y_{C,1}/M_C + \frac{1}{4}Y_{H,1}/M_H + \frac{1}{3}Y_{O,2}/M_O} \tag{28}$$

From Eq. (28), the stoichiometric value of Z is equal to

$$Z_{st} = \frac{Y_{O,2}/M_O}{\frac{1}{2}Y_{C,1}/M_C + \frac{1}{4}Y_{H,1}/M_H + \frac{1}{3}Y_{O,2}/M_O} \tag{29}$$

where Y_j and M_j are the mass fractions and atomic masses for the elements carbon, hydrogen, and oxygen. Subscripts

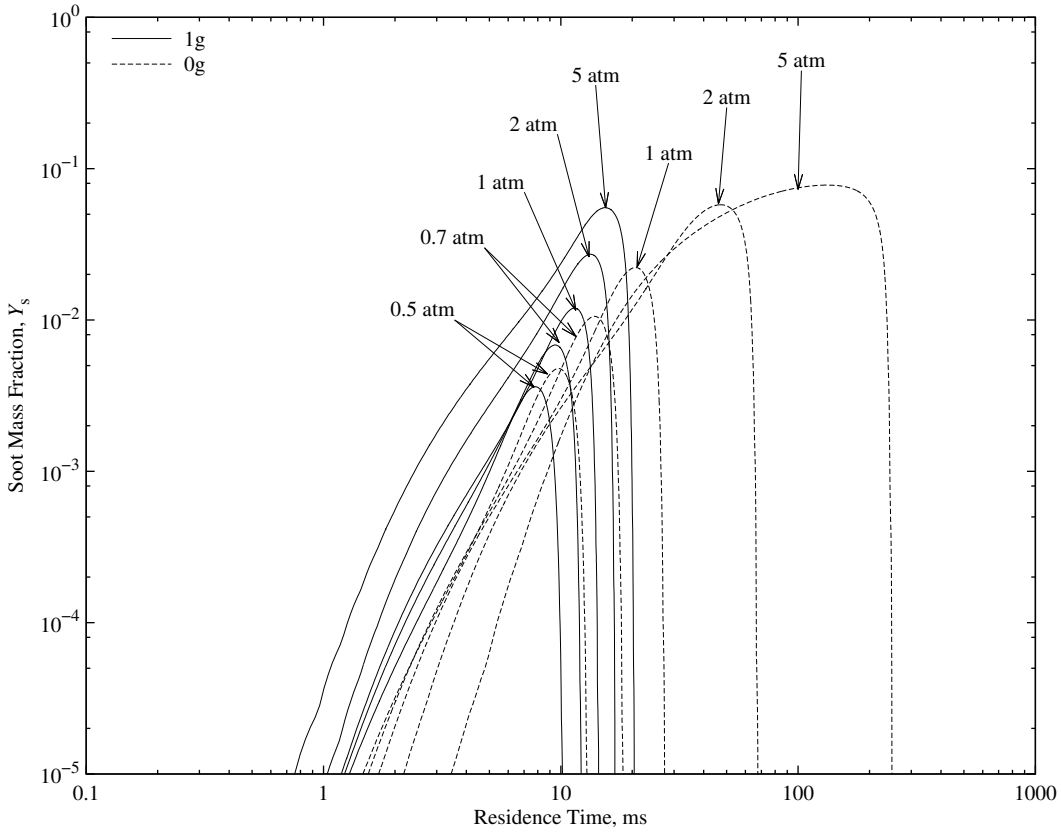

Figure 5. Soot mass fraction along a particle streamline originating from the reaction zone and passing through the maximum soot volume fraction.

1 and 2 refer to values in the fuel and air streams, respectively.

As observed in Fig. 5, the soot mass fraction initially increases with residence time, peaks, and rapidly decreases. At 0.5 atm, the differences between the normal- and zero-gravity flames are small. Residences times are similar and the peak soot mass fraction is only slightly enhanced at zero-gravity. Since soot levels are low and residence times do not increase much from normal to zero gravity at 0.5 atm, differences in predicted temperatures are expected to be small at this pressure. As such, the enhanced soot production which occurs in the 0.5 atm flame when gravity is neglected is attributed to longer residence times and reduced flow velocities. Reducing flow velocities slows the entrainment of fresh oxidizer into the flame, promoting pyrolysis and delaying soot oxidation.

For the normal-gravity cases, more soot is produced at elevated-pressures mainly because soot formation begins earlier and lasts longer. The soot formation rates, i.e., the slopes of the lines in Fig. 5, do not change much as pressure is increased. Soot formation takes more time to start when pressure is increased for the zero-gravity flames, but the soot yield still increases because the overall time from nucleation to complete destruction gets longer. This observed increase in residence time between 0.5–5 atm is significantly larger for the zero-gravity flames; a factor of 2 increase is observed at normal gravity while a factor of 20 increase occurs under zero-gravity conditions. This produces higher soot concentrations in zero gravity and results in the previously-mentioned enhanced dependence of η_s on pressure at low pressures. The lower zero-gravity dependence of η_s on pressure above 2 atm is attributed to a lack of available acetylene for further soot production and decreased temperatures. Radiative heat losses increase significantly above 1 atm in zero gravity since residence times increase with pressure-squared and soot levels are high.

The predicted contours of soot volume fraction for the flames at both levels of gravity are compared in Fig. 6. The location of the stoichiometric mixture fraction surface in each flame is also indicated in Fig. 6 to compare the effects of gravity and pressure on flame geometry. As observed in the figure, soot concentrations at each pressure are consistently higher for the zero-gravity flames. For example, the peak soot volume fraction in zero gravity is roughly 1.4, 1.6, 2.0, 2.7, and 2.2 times larger than the equivalent normal-gravity flame at 0.5, 0.7, 1, 2, and 5 atm, respectively. A similar factor-of-two enhancement of the peak soot volume fraction in micro-gravity was measured during drop-tower experiments [21,26,71] and predicted by Kong and Liu [36,37]. Kaplan et al. [18] predicted a much larger 11-fold increase

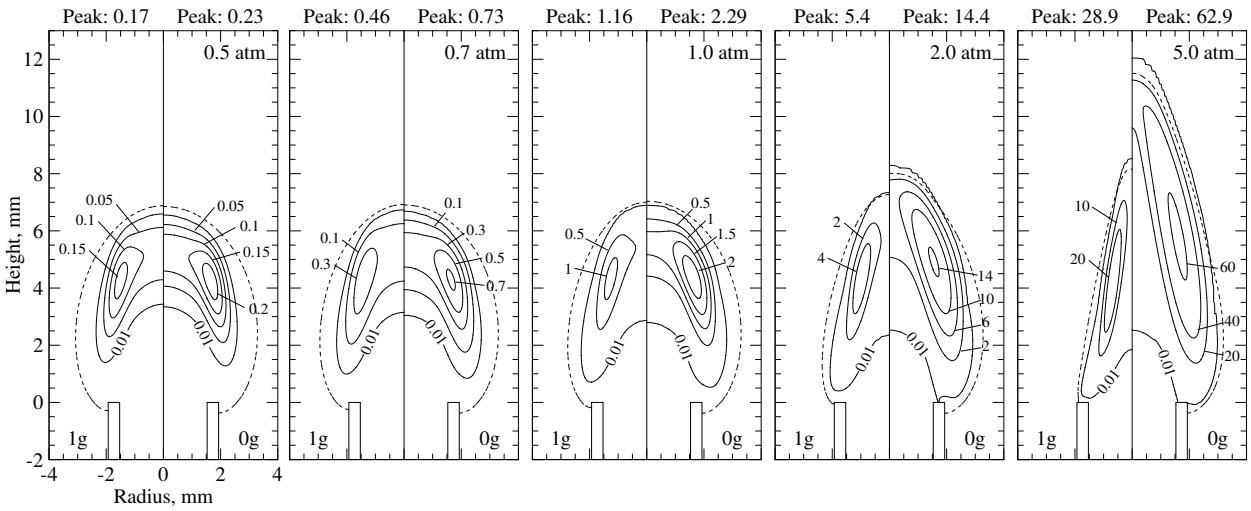

Figure 6. Predicted contours for soot volume fraction in the normal-gravity (left) and zero-gravity (right) flames. Units in ppm. Dashed black lines denote the location where the mixture fraction is equal to the stoichiometric value. Visible flame shape is denoted by the 0.01 ppm contour.

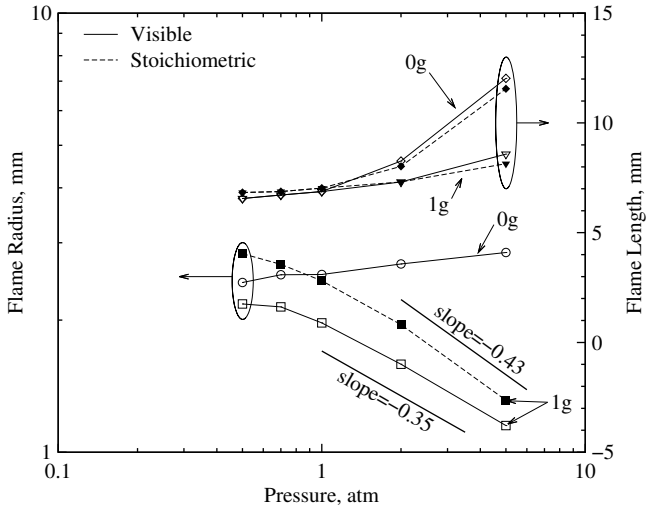

Figure 7. Effect of pressure and gravity on the computed flame shape. Flame radii correspond to an axial height of 4 mm.

in soot volume fraction for laminar ethylene-air jet diffusion flames in quiescent air. Between 0.5 and 1 atm, the predicted soot concentrations for each pressure have a similar structure under normal- and zero-gravity conditions except that soot is formed slightly lower in the zero-gravity flames. This earlier appearance of soot occurs primarily because velocities are slower and residence times longer for the zero-gravity cases. Above 1 atm, the heights of the zero-gravity flames become significantly longer than the normal-gravity flames since more soot is produced and oxidation rates are slower in zero-gravity.

There is a noticeable difference in the effect of pressure on flame structure at the two gravity levels. Under normal gravity, the annular soot-containing region becomes thinner and more pronounced as pressure is increased to 5 atm. However, thermophoretic forces become relatively more important in zero-gravity, especially at high pressures where flow velocities are low, which drive particles off flow streamlines and thicken the annular soot-containing region. The increased effects of molecular diffusion, which also become more important as pressures are increased in the absence of gravity, contribute to the thickening of the soot-containing region by widening the reaction zone.

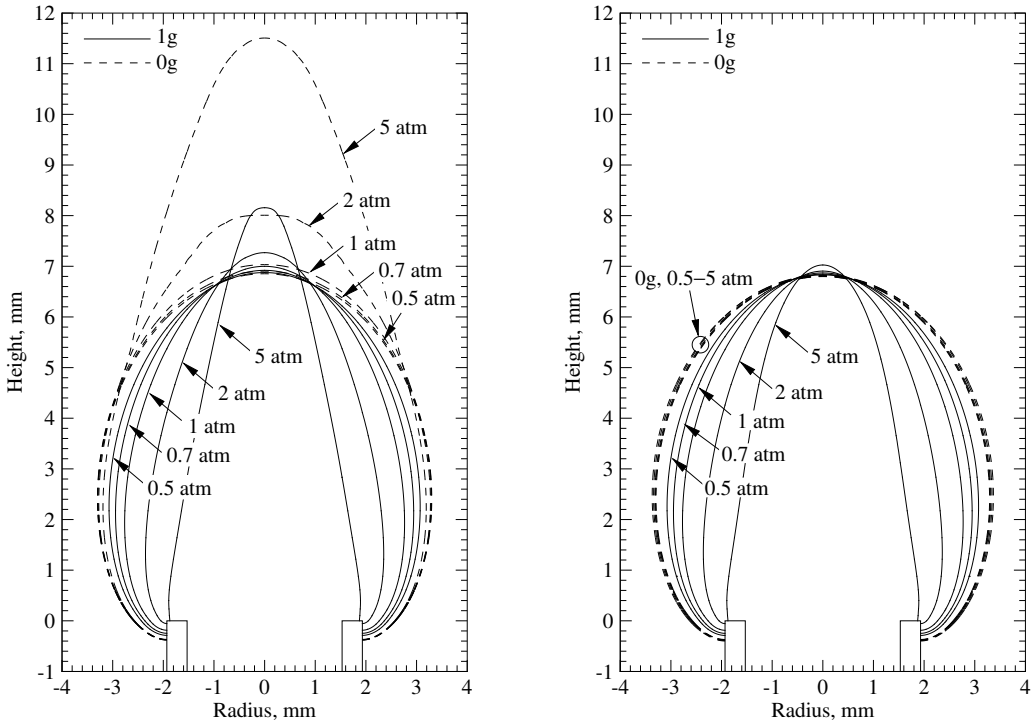

(a) soot and radiation included

(b) soot and radiation neglected

Figure 8. The effect of pressure and gravity on the stoichiometric mixture fraction surface.

B. Flame Geometry

The effect of pressure on flame shape, illustrated in Fig. 6, is different at normal- and zero-gravity. The shapes of the flames are similar when pressure is low, but deviate significantly as pressure is increased. For example, flame width decreases with increasing pressure at normal-gravity, in accordance with previous findings[4,5,7–9], while it increases with pressure at zero-gravity. The zero-gravity flames also become significantly longer than the normal-gravity ones above 1 atm. These observed differences are summarized in Fig. 7, which compares the computed flame lengths and radii for all flames. Two different methods were used to define the edge of the flame—based on the visible flame geometry and based on the stoichiometric mixture fraction. In this study, the visible edge of the flame is defined by the isocontour where soot volume fraction is equal to 0.01 ppm. At normal-gravity and high pressures, the visible and stoichiometric flame radii are proportional to $p^{-0.43}$ and $p^{-0.35}$, respectively. However, a much slower rate of decrease is observed between 0.5 to 2 atm since the effects of buoyancy weaken as pressure is decreased. Buoyant forces are not present in the zero-gravity cases and therefore soot transport via thermophoresis becomes increasingly important at high pressures where axial velocities are small. As a result, the visible widths of the zero-gravity flames increase proportional to $p^{0.07}$ over the entire range of pressures considered. The rapid increase in flame height between 1 and 5 atm at zero-gravity suggests that the 5 atm zero-gravity flame is close to the smoke point.

The strong effect of gravity and pressure on flame shape is illustrated in Fig. 8(a), which compares the predicted stoichiometric mixture fraction isocontours for each flame. Gravity has absolutely no effect on the flame height when soot and radiation are turned off, Fig. 8(b). This implies that the lengthening of the zero-gravity flames with pressures occurs solely because of the reduced flame temperatures and slower oxidation of soot.

C. Residence Time and Velocity

Under normal-gravity conditions, pressure should not affect the residence times in buoyancy-dominated laminar diffusion flames (see discussion in Section I). However, as observed in Fig. 5, the particle residence time increases with pressure regardless of gravity level. While this change in residence time is expected for zero-gravity conditions because there are no buoyant forces to accelerate the flow, it is not clear why residence time increases at normal gravity. Under zero-gravity conditions, the axial velocity along the centerline, illustrated in Fig. 9(a), decreases almost linearly

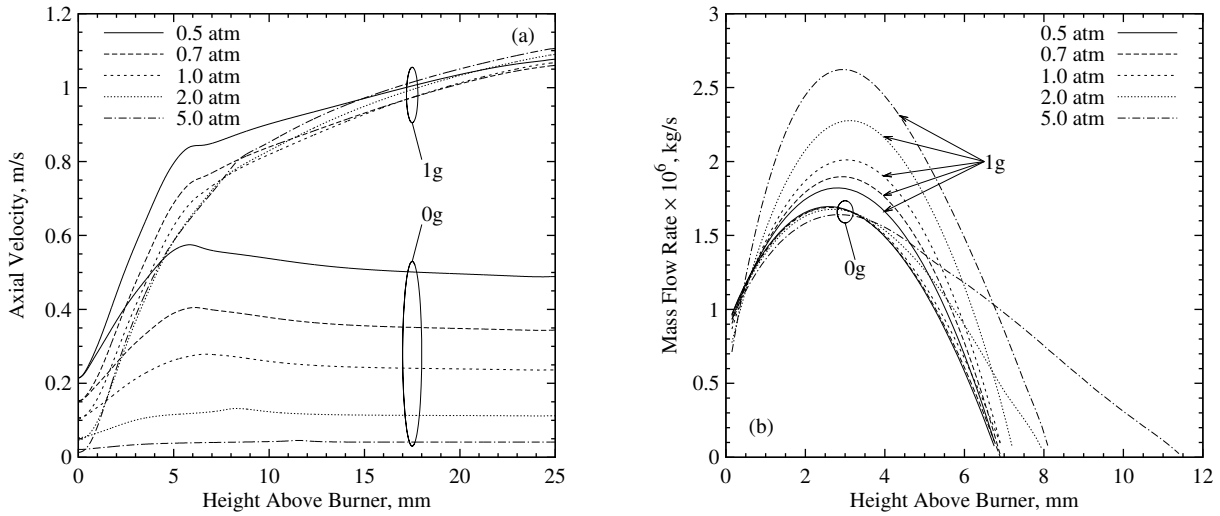

Figure 9. (a) Distributions of the predicted axial velocity along the flame centerline and (b) the mass flow rate through the stoichiometric flame envelope.

with pressure. However, the centerline velocities for the normal-gravity flames do not change much with pressure because buoyant forces quickly accelerate the flow. Thus, the change in residence time with increasing pressure at normal gravity occurs because the flame diameter is approximately proportional to $p^{-0.4}$ instead of $p^{-0.5}$ (the theoretical relationship). This leads to lower average velocities through the core of the flame and longer residence times under normal-gravity conditions. It suggests that the ethylene-flames studied here are still developing and not fully buoyancy dominated, even at 5 atm. This development is observed in Fig. 7 since the relationship between pressure and flame diameter appears to be changing asymptotically. These results would also explain the increase in flame height observed as pressure is increased under normal-gravity conditions.

Oddly, the mass flow rate through the flame envelope actually increases with pressure under normal-gravity conditions, illustrated in Fig. 9(b). For this study, the flame envelope is defined by the isocontour where the mixture fraction is stoichiometric. The mass flow decreases beyond about 3 mm since the flame begins to close. Under normal-gravity conditions, more of the surrounding coflow is entrained into the flame at higher pressures because the velocity of the surrounding air decreases while the velocity of the central core remains roughly constant. This creates an intense shear-layer between the two streams. The mass flow rate through the zero-gravity flames is unaffected by pressure, possibly because the flame diameter doesn't change and the velocities of the two streams both decrease at the same rate with pressure. The results shown in Fig. 9 indicate that residence time cannot always be assumed independent of pressure, at least at lower pressures.

D. Temperature and Radiation Heat Transfer

The predicted temperature contours for the normal- and zero-gravity flames are compared in Fig. 10(a). Temperature predictions were also computed neglecting soot and radiation, Fig. 10(b), to assess the impact of radiation on flame structure. At 0.5 atm, there is almost no difference between the predicted temperature fields at the two levels of gravity since the effects of radiation are small. However, radiation effects become large as pressure is increased to 5 atm which drastically alters the predicted temperature fields in both the normal- and zero-gravity flames. Residence times do not change much in the normal-gravity flames and, as such, radiation is primarily influenced by the local soot concentrations. Increasing pressure has a much larger effect on radiation when gravity is absent as residence times are drastically increased and soot production is enhanced. This is evident by comparing the results computed with and without radiation, Figs. 10(a) and 10(b).

Considering the temperature predictions obtained without soot and radiation, Fig. 10(b), peak temperatures steadily increase with pressure. Temperatures are only marginally lower in zero gravity since the transport of fresh reactants to the reaction zone is slower. When soot and radiation are included, Fig. 10(a), peak temperatures of the normal-gravity flames increase with pressure at a slower rate since any increase in heat-release is counter-acted by radiative heat losses. Radiation effects are much stronger at zero gravity due to the increased residence time and, as a result, peak

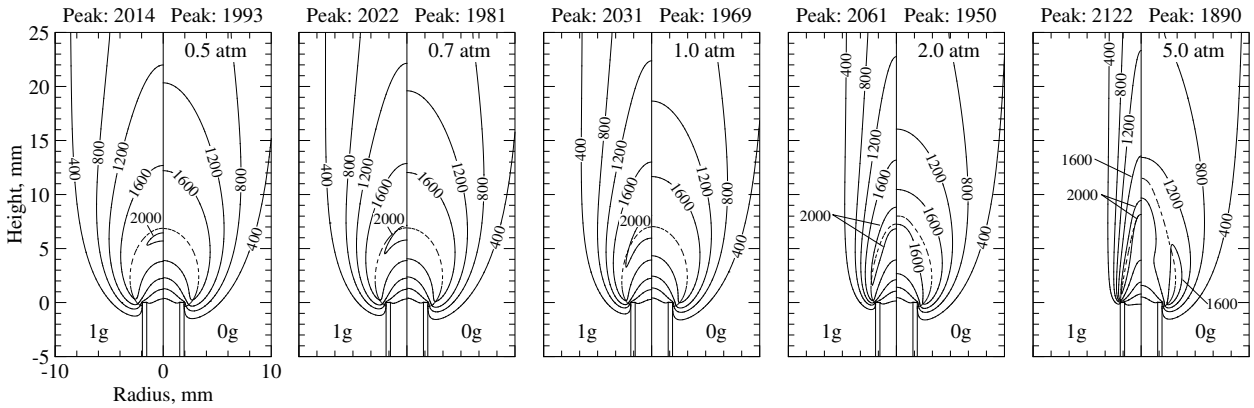

(a) soot and radiation included

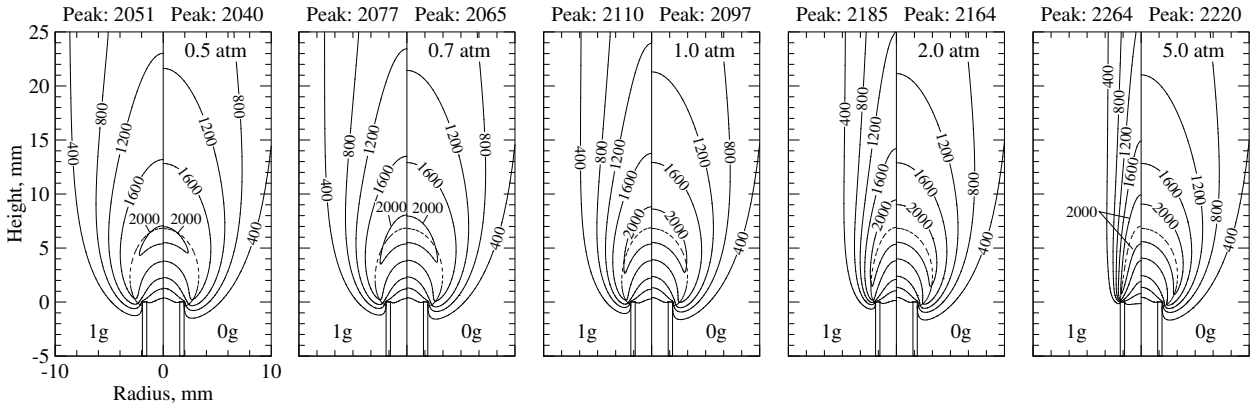

(b) soot and radiation neglected

Figure 10. Predicted temperature contours for the normal-gravity (left) and zero-gravity (right) flames. Units in K. The dashed black lines correspond to the location where the mixture fraction is equal to the stoichiometric value.

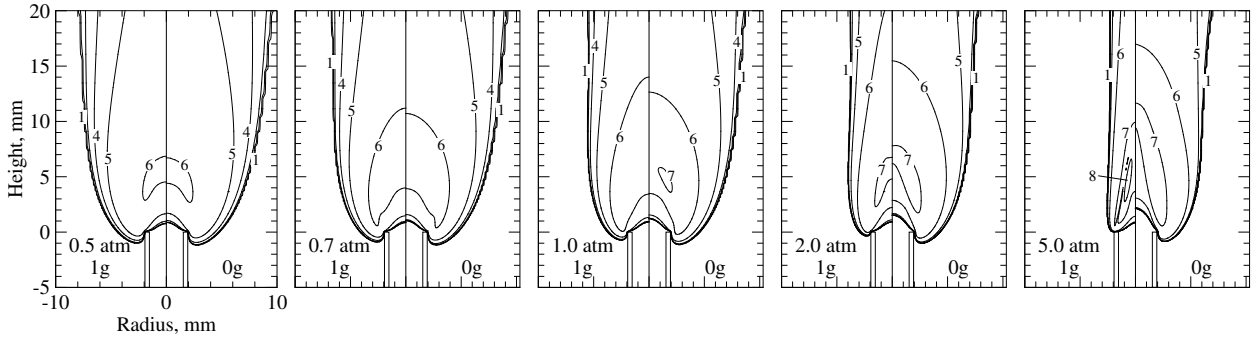

Figure 11. Predicted contours of the divergence of the radiative heat flux, $\nabla \cdot \mathbf{q}_{\mathbf{rad}}$. Contours correspond to $\log_{10}\left[\max\left(-\nabla \cdot \mathbf{q}_{\mathbf{rad}}\right), 1\right]$.

temperatures decrease with increasing pressure. Above 1 atm, the peak temperatures in the zero-gravity flames are significantly lower than those in the normal-gravity flames. There is also a considerable temperature drop along the centerline in zero-gravity. These low temperatures in the zero-gravity flames are one of the primary reasons for the decreased sensitivity of η_s to pressure observed above 1 atm.

The divergence of the radiative heat flux, $\nabla \cdot \mathbf{q}_{\mathrm{rad}}$, is plotted in Fig. 11 for each flame. Since this quantity varies exponentially over the range of pressures studied, the logarithm of the negative component of $\nabla \cdot \mathbf{q}_{\mathrm{rad}}$ is plotted in Fig. 11. At 0.5 atm, the predicted contours of $\nabla \cdot \mathbf{q}_{\mathrm{rad}}$ at normal- and zero-gravity conditions are very similar. However, the rapid increase in radiation transport with pressure produces significant differences between the predictions for $\nabla \cdot \mathbf{q}_{\mathrm{rad}}$

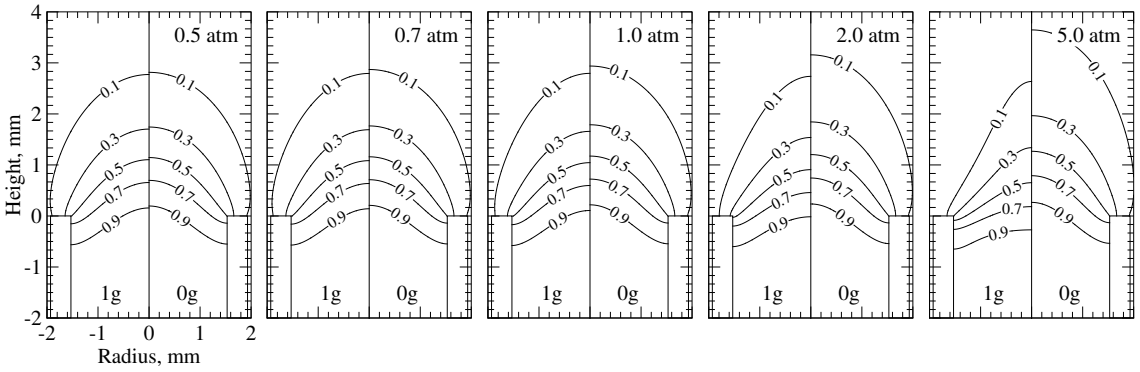

Figure 12. Predicted contours for ethylene mass fraction in the normal-gravity (left) and zero-gravity (right) flames.

in the two 5 atm flames. The magnitude of $\nabla \cdot \mathbf{q}_{\text{rad}}$ is larger in the zero-gravity flames below 2 atm but becomes larger in the normal-gravity flame at 5 atm. This is a direct result of the steeper temperature and soot concentration gradients in the normal-gravity flames at high pressures. There is also a significant amount of energy transported upstream into the coflow air supply tube. While this upstream energy transport vanishes under normal-gravity conditions when pressure is increased to 5 atm, it intensifies with pressure in the absence of gravity.

E. Species Mass Fractions

In the presence of gravity, buoyant forces rapidly accelerate the flow upward, entraining the surrounding co-flowing oxidizer stream and mixing the oxidizer with fresh fuel. Since buoyancy-induced acceleration scales with $p^2 g$, increasing pressure intensifies entrainment and speeds up oxidative pyrolysis. This phenomenon is observed in Fig. 12, which shows the predicted contours of ethylene mass fraction in the normal- and zero-gravity flames. For normal-gravity conditions, ethylene is consumed at a faster rate as pressure is increased from 0.5 to 5 atm. Early fuel pyrolysis is also observed inside the fuel tube at high pressures. When gravity is eliminated, increasing pressure while maintaining fixed mass flow rates has the opposite effect since flow velocities are reduced. As such, convective transport slows and fuel consumption rates decrease. No early fuel pyrolysis is observed at zero-gravity due to the lower centerline temperatures which were observed in Fig. 10(a).

The predicted acetylene mass fractions for all of the flames studied are illustrated in Fig. 13(a). Acetylene concentrations steadily decrease as pressure is increased from 0.5 to 5 atm in both cases, normal- and zero-gravity, which is attributed to the consumption of acetylene to produce soot. This is confirmed by Fig. 13(b), which shows the predicted acetylene mass fractions computed when soot and radiation are neglected. The observed decrease in acetylene mass fraction with increasing pressure is substantially larger when gravity is neglected due to the long residence times and enhanced soot production. The low temperatures observed in Fig. 10(a) along the centerline under zero gravity may also hinder the production of acetylene. These significantly lower acetylene concentrations above 1 atm in zero gravity contribute to the weaker η_s-pressure dependence observed when gravity is eliminated. Between 0.5 and 1 atm, acetylene concentrations and temperatures are similar at both levels of gravity, so the stronger η_s-pressure dependence in zero-gravity is caused by the effect of pressure on velocity and residence time.

VI. Influence of Wall Boundary Condition

Panek and Gülder [33] observed a blue region at the base of the flame that vanished as pressure was increased to 5 atm. At this pressure, the yellow luminous portion of the flame extended from the flame tip all the way to the burner rim. Large gradients occur near the fuel tube rim, which were discussed in the previous sections, and significant heating of the fuel tube is expected as a result. The temperatures along the outer surface of the burner tube were measured by Gülder et al. [72] for laminar coflow diffusion flames of ethylene and propylene at atmospheric pressure. They reported fuel tube temperatures up to 100 K higher than the temperature of the fresh reactants. Based on the visual observations of Panek and Gülder [33] and the numerical results discussed in previous sections, this heating of the tube rim is expected to intensify as the flame base moves towards the burner rim with increasing pressure.

In order to assess the effect of gas-tube heat transfer on the numerical predictions, additional calculations were performed at 5 atm using an adiabatic boundary condition for the tube walls. Specifying adiabatic walls represents the

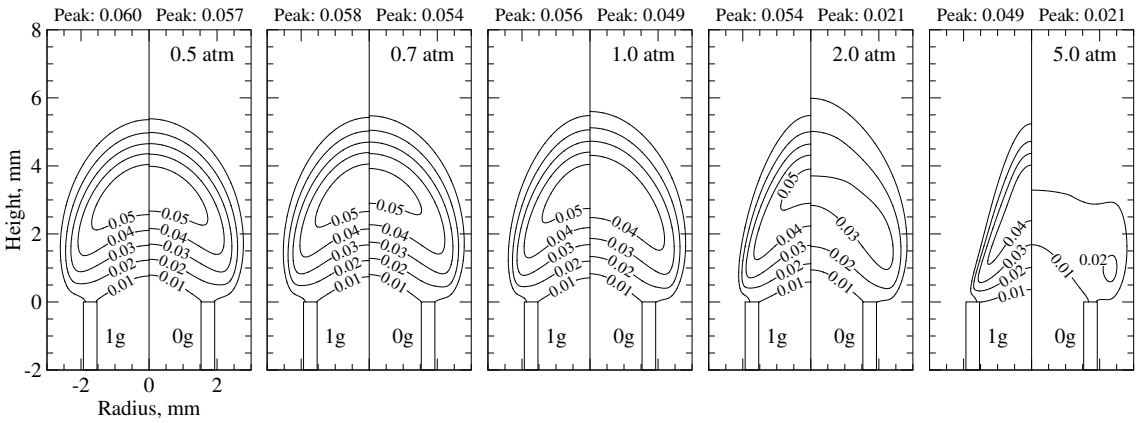

(a) soot and radiation included

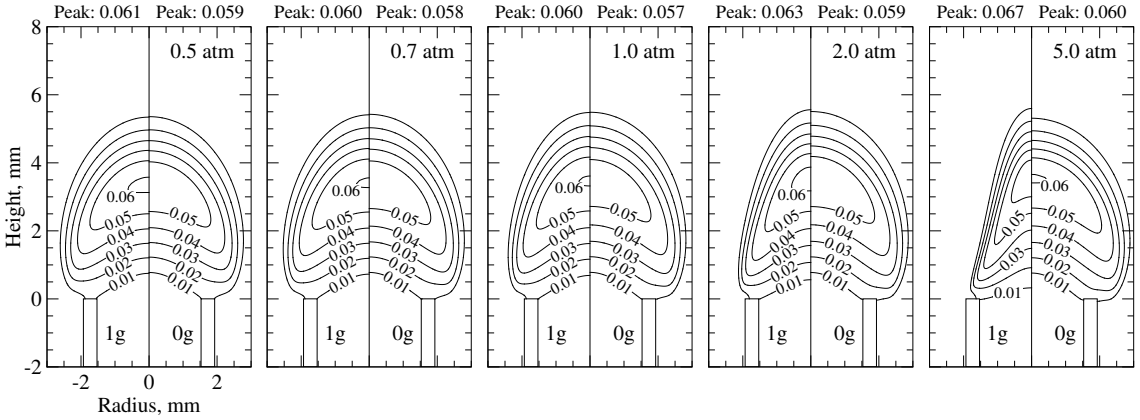

(b) soot and radiation neglected

Figure 13. Predicted contours for acetylene mass fraction in the normal-gravity (left) and zero-gravity (right) flames.

opposite limit with respect to the effects of wall heating since the tube is allowed to heat up to the maximum possible temperature. The true boundary condition lies somewhere in between the two extremes.

The predicted soot volume fraction and temperature contours computed using the new boundary conditions are provided in Fig. 14 for the two flames. Changing the wall boundary condition significantly alters the numerical predictions; soot concentrations are larger and the visible flame heights of the two flames are longer in the absence of gas-tube heat transfer. Peak soot concentrations are 2.4 and 1.8 times larger using the adiabatic boundary conditions at normal and zero gravity, respectively. This increase in predicted soot volume fraction is attributed to the higher temperatures near the flame base which result when the walls are adiabatic. For adiabatic walls, temperatures exceed 2000 K near the tip of the tube in both cases. As such, soot production rates near the tube wall intensify and more soot is produced throughout the flame. For the normal-gravity flame, the new calculations over-predicted the measured soot concentrations shown in Figs. 2 and 3 by about the same amount as they were under-predicted before. The newly predicted visible flame length is approximately 9.5 mm which is in better agreement with the experimental observations. When adiabatic walls are specified, the zero-gravity flame begins to emit smoke since soot is no longer fully oxidized before leaving the flame envelope. Changing the boundary condition also causes the peak soot volume fraction in zero-gravity flame to shift to the centerline.

Comparing the predictions for temperature in Figs. 10(a) and 14, the peak values are 120 and 164 K larger at normal- and zero-gravity conditions, respectively, when adiabatic walls are specified as opposed to a fixed wall temperature. These peak values occur lower in the flame near the tip of the fuel tube. normal- and zero-gravity, respectively, when adiabatic walls are specified. These peak values occur lower in the flame near the tip of the fuel tube. There is also a dramatic decrease in temperature along the centerline at zero-gravity since radiative heat losses are enhanced by the higher soot concentrations.

To conclude this discussion, it should be noted that the agreement between predictions and measurements for

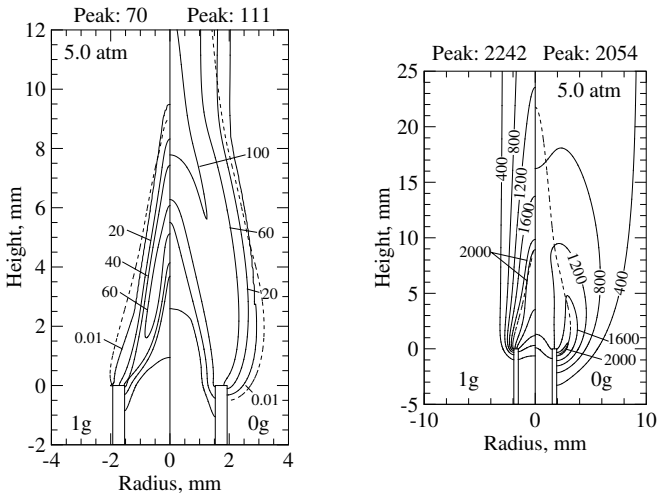

Figure 14. Soot volume fraction (left) and temperature (right) contours computed using an adiabatic wall boundary condition. Soot volume fraction in ppm and temperature in K. Dashed black lines denote the location where the mixture fraction is equal to the stoichiometric value.

temperature and soot volume fraction did not improve when the adiabatic wall boundary condition was employed.

VII. Conclusions

The ethylene laminar coflow diffusion flames of Panek and Gülder[33] were investigated numerically to assess the predictive capabilities of a simple, acetylene-based soot model and help explain a number of the experimental findings. Additional calculations were performed without gravity to isolate the effects of buoyancy and pressure on sooting characteristics and flame structure. Values for pressure considered ranged from 0.5 to 5 atm.

Predictions for soot volume fraction and temperature in the normal-gravity flames differed significantly from the measurements. These differences were attributed to experimental errors at low pressures, errors introduced by the acetylene-based soot model[40], and uncertainties in the boundary conditions. Nonetheless, the soot model captured the increase in maximum η_s with pressure and the decreased sensitivity of η_s to pressure above 1 atm. Due to deficiencies of acetylene-based soot models[9], this dependence of η_s on pressure was under-estimated over the entire range of pressures investigated. Future research will consider more realistic physical models for soot that describe the formation of large molecular weight soot precursors[73] and include advanced descriptions for aerosol dynamics[74,75].

Based on the numerical results, pressure and gravity were observed to significantly influence the sooting behaviour and flame structure of laminar diffusion flames. Zero-gravity flames were shown to have higher soot concentrations, lower temperatures, and thicker soot-containing regions than normal-gravity flames at the same pressure. Different behaviour was observed under normal- and zero-gravity conditions when pressure was increased from 0.5 to 5 atm. The zero-gravity flames displayed a stronger η_s-pressure dependence between 0.5 to 2 atm and a weaker dependence between 2 to 5 atm. An investigation of the numerical results has revealed that these differences in the soot-pressure dependence is a result of several factors. At low pressures, the predicted temperatures and acetylene mass fractions for flames at the two levels of gravity are similar because soot volume fractions are low and the effects of buoyancy are minimized. As a result, the η_s-pressure dependence is strengthened in zero gravity by the effect of pressure on residence time. However, residence times become longer and soot volume fractions higher as pressure is increased above 1 atm in the absence of gravity, promoting large radiation losses and reducing temperatures. This causes soot production rates to decrease and results in the weaker η_s-pressure dependence displayed by the zero-gravity flames. This dependence is also weakened by the lower availability of acetylene in zero gravity.

Flame shape was observed to change when gravity and pressure were varied. Zero-gravity flames are generally longer and wider, and they display a different relationship between shape and pressure than the same flames under normal-gravity conditions. Flame diameter decreases with increasing pressure in normal gravity while it increases with pressure in zero gravity. There is also a larger increase in flame length from 1 to 5 atm in zero gravity.

Changing the prescribed wall boundary condition was observed to affect the numerical predictions at 5 atm. When adiabatic boundary conditions were used instead of cold walls, temperatures and soot volume fractions were higher.

The visible flame length was also longer. These results indicate that wall temperatures are somewhere in-between the reactant stream temperature and the adiabatic flame temperature. Future calculations should incorporate a conjugate heat transfer analysis of the tube walls to enhance the accuracy of the predictions.

Acknowledgments

We thank Natalie Panek for providing assistance with the experimental data. Operational funds for this work have been provided by the Natural Sciences and Engineering Research Council (NSERC) and the Canadian Space Agency (CSA). Computational resources for performing all of the calculations reported herein were provided by the SciNet High Performance Computing Consortium at the University of Toronto and Compute/Calcul Canada through funding from the Canada Foundation for Innovation (CFI) and the Province of Ontario, Canada.

References

[1]Miller, I. M. and Maahs, H. G., "High-Pressure Flame Systems for Pollution Studies with Results for Methane-Air Diffusion Flames," TN D-8407, NASA, 1977.

[2]Flower, W. L. and Bowman, C. T., "Soot production in axisymmetric laminar diffusion flames at pressures from one to ten atmospheres," *Proceedings of the Combustion Institute*, Vol. 21, No. 1, 1988, pp. 1115–1124.

[3]Greenberg, P. S., "Laser Doppler velocimetry and full-field soot volume fraction measurements in microgravity," *Proceedings of the 3rd International Microgravity Combustion Workshop*, NASA, Cleveland, OH, April 10–13 1995, pp. 247–252.

[4]McCrain, L. L. and Roberts, W. L., "Measurements of the soot volume field in laminar diffusion flames at elevated pressures," *Combustion and Flame*, Vol. 140, 2005, pp. 60–69.

[5]Thomson, K. A., Gülder, Ö. L., Weckman, E. J., Fraser, R. A., Smallwood, G. J., and Snelling, D. R., "Soot concentration and temperature measurements in co-annular, nonpremixed CH_4/air laminar flames at pressures up to 4 MPa," *Combustion and Flame*, Vol. 140, 2005, pp. 222–232.

[6]Glassman, I., "Sooting laminar diffusion flames: effect of dilution, additives, pressure, and microgravity," *Proceedings of the Combustion Institute*, Vol. 27, 1998, pp. 1589–1596.

[7]Bento, D. S., Thomson, K. A., and Gülder, Ö. L., "Soot formation and temperature field structure in laminar propane-air diffusion flames at elevated pressures," *Combustion and Flame*, Vol. 145, 2006, pp. 765–778.

[8]Joo, H. I. and Gülder, Ö. L., "Soot formation and temperature field structure in co-flow laminar methane-air diffusion flames at pressures from 10 to 60 atm," *Proceedings of the Combustion Institute*, Vol. 32, No. 1, 2009, pp. 769–775.

[9]Liu, F., Thomson, K., Guo, H., and Smallwood, G. J., "Numerical and experimental study of an axisymmetric coflow laminar methane-air diffusion flame at pressures between 5 and 40 atmospheres," *Combustion and Flame*, Vol. 146, 2006, pp. 456–471.

[10]Roper, F. G., "The prediction of laminar jet diffusion flame sizes: Part I. Theoretical model," *Combustion and Flame*, Vol. 29, 1977, pp. 219–226.

[11]Roper, F. G., Smith, C., and Cunningham, A. C., "The prediction of laminar jet diffusion flame sizes: Part II. Experimental verification," *Combustion and Flame*, Vol. 29, 1977, pp. 227–234.

[12]Charest, M. R. J., Joo, H. I., Gülder, Ö. L., and Groth, C. P. T., "Experimental and numerical study of soot formation in laminar ethylene diffusion flames at elevated pressures from 10 to 35 atm," *Proceedings of the Combustion Institute*, Vol. 33, 2010, doi:10.1016/j.proci.2010.07.054.

[13]Cochran, T. H., "Experimental investigation of laminar gas jet diffusion flames in zero gravity," Tech. rep., NASA-TN-D-6523, 1972.

[14]Haggard, Jr, J. B., "Forced and natural convection in laminar-jet diffusion flames," Tech. rep., NASA-TP-1841, 1981.

[15]Lin, K. C., Faeth, G. M., Sunderland, P. B., Urban, D. L., and Yuan, Z. G., "Shapes of nonbuoyant round luminous hydrocarbon/air laminar jet diffusion flames," *Combustion and Flame*, Vol. 116, No. 3, 1998, pp. 415–431.

[16]Sunderland, P. B., Mendelson, B. J., Yuan, Z. G., and Urban, D. L., "Shapes of buoyant and nonbuoyant laminar jet diffusion flames," *Combustion and Flame*, Vol. 116, No. 3, 1999, pp. 376–386.

[17]Lee, W. and Na, Y. D., "Soot study in laminar diffusion flames at elevated pressures using two-color pyrometry and Abel inversion," *JSME International Journal Series B*, Vol. 43, No. 4, 2000, pp. 550–555.

[18]Kaplan, C. R., Oran, E. S., Kailasanath, K., and Ross, H. D., "Gravitational effects on sooting diffusion flames," *Proceedings of the Combustion Institute*, Vol. 26, No. 1, 1996, pp. 1301–1309.

[19]Sunderland, P. B., Mortazavi, S., Faeth, G. M., and Urban, D. L., "Laminar smoke points of nonbuoyant jet diffusion flames," *Combustion and Flame*, Vol. 96, No. 1-2, 1994, pp. 97–103.

[20]Ku, J. C., Griffin, D. W., Greenberg, P. S., and Roma, J., "Buoyancy-induced differences in soot morphology," *Combustion and Flame*, Vol. 102, No. 1-2, 1995, pp. 216–218.

[21]Reimann, J. and Will, S., "Optical diagnostics on sooting laminar diffusion flames in microgravity," *Microgravity Science and Technology*, Vol. 15, No. 1, 2005, pp. 333–337.

[22]Urban, D. L., Yuan, Z. G., Sunderland, P. B., Lin, K. C., Dai, Z., and Faeth, G. M., "Smoke-point properties of non-buoyant round laminar jet diffusion flames," *Proceedings of the Combustion Institute*, Vol. 28, No. 2, 2000, pp. 1965–1971.

[23]Sunderland, P. B., Köylü, Ü. Ö., and Faeth, G. M., "Soot formation in weakly buoyant acetylene-fueled laminar jet diffusion flames burning in air," *Combustion and Flame*, Vol. 100, No. 1-2, 1995, pp. 310–322.

[24]Sunderland, P. B. and Faeth, G. M., "Soot nucleation and growth in weakly-bouyant hydrocarbon diffusion flames," Tech. rep., AIAA-1995-149, 1995.

[25]Sunderland, P. B. and Faeth, G. M., "Soot formation in hydrocarbon/air laminar jet diffusion flames," *Combustion and Flame*, Vol. 105, No. 1-2, 1996, pp. 132–146.

[26]Greenberg, P. S. and Ku, J. C., "Soot volume fraction maps for normal and reduced gravity laminar acetylene jet diffusion flames," *Combustion and Flame*, Vol. 108, No. 1-2, 1997, pp. 227–230.

[27]Vander Wal, R. L., "Laser-induced incandescence measurements in low-gravity," *Microgravity Science and Technology*, Vol. 10, No. 2, 1997, pp. 66–74.

[28]Walsh, K. T., Fielding, J., Smooke, M. D., and Long, M. B., "Experimental and computational study of temperature, species, and soot in buoyant and non-buoyant coflow laminar diffusion flames," *Proceedings of the Combustion Institute*, Vol. 28, No. 2, 2000, pp. 1973–1979.

[29]Urban, D. L., Yuan, Z. G., Sunderland, P. B., Linteris, G. T., Voss, J. E., Lin, K. C., Dai, Z., Sun, K., and Faeth, G. M., "Structure and soot properties of nonbuoyant ethylene/air laminar jet diffusion flames," *AIAA Journal*, Vol. 36, No. 8, 1998, pp. 1346–1360.

[30]Lin, K. C., Dai, Z., and Faeth, G. M., "Laminar soot processes," *Fifth International Microgravity Combustion Workshop*, NASA, Cleveland, OH, May 18–20 1999, pp. 147–150.

[31]Diez, F. J., Aalburg, C., Sunderland, P. B., Urban, D. L., Yuan, Z. G., and Faeth, G. M., "Soot properties of laminar jet diffusion flames in microgravity," *Combustion and Flame*, Vol. 156, No. 8, 2009, pp. 1514–1524.

[32]Law, C. K. and Faeth, G. M., "Opportunities and challenges of combustion in microgravity," *Progress in Energy and Combustion Science*, Vol. 20, No. 1, 1994, pp. 65–113.

[33]Panek, N. and Gülder, Ö. L., "Simulation of microgravity diffusion flames using sub-atmospheric pressures," *48th AIAA Aerospace Sciences Meeting*, Orlando, Florida, 4–7 January 2010, AIAA 2010-1477.

[34]Ezekoye, O. A. and Zhang, Z., "Soot oxidation and agglomeration modeling in a microgravity diffusion flame," *Combustion and Flame*, Vol. 110, 1997, pp. 127–139.

[35]Legros, G., Fuentes, A., Rouvreau, S., Joulain, P., Porterie, B., and Torero, J. L., "Transport mechanisms controlling soot production inside a non-buoyant laminar diffusion flame," *Proceedings of the Combustion Institute*, Vol. 32, No. 2, 2009, pp. 2461–2470.

[36]Kong, W. and Liu, F., "Numerical study of the effects of gravity on soot formation in laminar coflow methane/air diffusion flames under different air stream velocities," *Combustion Theory and Modelling*, Vol. 13, No. 6, 2009, pp. 993–1023.

[37]Kong, W. and Liu, F., "Effects of gravity on soot formation in a coflow laminar methane/air diffusion flame," *Microgravity Science and Technology*, Vol. 22, No. 2, 2010, pp. 205–214.

[38]Zhang, Z. and Ezekoye, O. A., "Soot production rate calculations at elevated pressure in a methane-air jet jet diffusion flame," *Combustion Science and Technology*, Vol. 137, 1998, pp. 323–346.

[39]Leung, K. M., Lindstedt, R. P., and Jones, W. P., "A simplified reaction mechanism for soot formation in nonpremixed flames," *Combustion and Flame*, Vol. 87, 1991, pp. 289–305.

[40]Liu, F., Guo, H., Smallwood, G. J., and Gülder, Ö. L., "Effects of gas and soot radiation on soot formation in a coflow laminar ethylene diffusion flame," *Journal of Quantitative Spectroscopy & Radiative Transfer*, Vol. 73, 2002, pp. 409–421.

[41]Charest, M. R. J., Groth, C. P. T., and Gülder, Ö. L., "A computational framework for predicting laminar reactive flows with soot formation," *Combustion Theory and Modelling*, Vol. 14, No. 6, 2010, pp. 793–825.

[42]Kuo, K. K., *Principles of Combustion*, John Wiley & Sons, Inc., New Jersey, 2nd ed., 2005.

[43]Fairweather, M., Jones, W. P., and Lindstedt, R. P., "Predictions of radiative transfer from a turbulent reacting jet in a cross-wind," *Combustion and Flame*, Vol. 89, 1992, pp. 45–63.

[44]Hirschfelder, J. O., Curtiss, C. F., and Byrd, R. B., *Molecular Theory of Gases and Liquids*, John Wiley & Sons, New York, 1969.

[45]Gomez, A. and Rosner, D. E., "Thermophoretic effects on particles in counterflow laminar diffusion flames," *Combustion Science and Technology*, Vol. 89, No. 5-6, 1993, pp. 335–362.

[46]Smooke, M. D., McEnally, C. S., Pfefferle, L. D., Hall, R. J., and Colket, M. B., "Computational and experimental study of soot formation in a coflow, laminar diffusion flame," *Combustion and Flame*, Vol. 117, 1999, pp. 117–139.

[47]Kennedy, I. M., Kollmann, W., and Chen, J. Y., "A model for the soot formation in a laminar diffusion flame," *Combustion and Flame*, Vol. 81, 1990, pp. 73–85.

[48]Nagle, J. and Strickland-Constable, R. F., "Oxidation of carbon between 1000-2000°C," *Proceedings of the Fifth Conference on Carbon*, Pergamon Press, London, 1962, pp. 154–164.

[49]Moss, J. B., Stewart, C. D., and Young, K. J., "Modeling soot formation and burnout in a high temperature laminar diffusion flame burning under oxygen-enriched conditions," *Combustion and Flame*, Vol. 101, 1995, pp. 491–500.

[50]Bradley, D., Dixon-Lewis, G., Habik, S. E., and Mushi, E. M. J., "The oxidation of graphite powder in flame reaction zones," *Proceedings of the Combustion Institute*, Vol. 20, 1984, pp. 931–940.

[51]Carlson, B. G. and Lathrop, K. D., "Transport theory - The method of discrete ordinates," *Computing Methods in Reactor Physics*, edited by H. Greenspan, C. N. Kelber, and D. Okrent, Gordon and Breach, London, 1968, pp. 171–266.

[52]Thurgood, C. P., Pollard, A., and Becker, H. A., "TN quadrature set for the discrete ordinates method," *Journal of Heat Transfer*, Vol. 117, No. 4, 1995, pp. 1068–1070.

[53]Liu, F., Smallwood, G. J., and Gülder, Ö. L., "Band lumping strategy for radiation heat transfer calculations using a narrowband model," *Journal of Thermophysics and Heat Transfer*, Vol. 14, No. 2, 2000, pp. 278–281.

[54]Liu, F., Smallwood, G. J., and Gülder, Ö. L., "Application of the statistical narrow-band correlated-k method to low-resolution spectral intensity and radiative heat transfer calculations - effects of the quadrature scheme," *International Journal of Heat and Mass Transfer*, Vol. 43, No. 17, 2000, pp. 3119–3135.

[55]Liu, F., Guo, H., and Smallwood, G. J., "Effects of radiation model on the modeling of a laminar coflow methane/air diffusion flame," *Combustion and Flame*, Vol. 138, No. 1-2, 2004, pp. 136–154.

[56]Soufiani, A. and Taine, J., "High temperature gas radiative property parameters of statistical narrow-band model for H_2O, CO_2 and CO, and correlated-K model for H_2O and CO_2," *International Journal of Heat and Mass Transfer*, Vol. 40, No. 4, 1997, pp. 987–991.

[57]Liu, F., Smallwood, G. J., and Gülder, Ö. L., "Application of the statistical narrow-band correlated-k method to non-grey gas radiation in CO_2-H_2O mixtures: Approximate treatments of overlapping bands," *Journal of Quantitative Spectroscopy & Radiative Transfer*, Vol. 68, No. 4, 2001, pp. 401–417.

[58]Goutiere, V., Charette, A., and Kiss, L., "Comparative performance of nongray gas modeling techniques," *Numerical Heat Transfer Part B*, Vol. 41, No. 3-4, 2002, pp. 361–381.

[59]Northrup, S. A. and Groth, C. P. T., "Solution of Laminar Combusting Flows Using a Parallel Implicit Adaptive Mesh Refinement Algorithm," *Proceedings of the Fourth International Conference on Computational Fluid Dynamics, ICCFD4*, Ghent, Belgium, July 10-14 2006, pp. 341–346.

[60]Gao, X. and Groth, C. P. T., "A parallel adaptive mesh refinement algorithm for predicting turbulent non-premixed combusting flows," *International Journal of Computational Fluid Dynamics*, Vol. 20, No. 5, 2006, pp. 349–357.

[61]Roe, P. L., "Approximate Riemann solvers, parameter vectors, and difference schemes," *Journal of Computational Physics*, Vol. 43, 1981, pp. 357–372.

[62]Coirier, W. J. and Powell, K. G., "Solution-Adaptive Cartesian Cell Approach for Viscous and Inviscid Flows," *AIAA Journal*, Vol. 34, No. 5, May 1996, pp. 938–945.

[63]Weiss, J. M. and Smith, W. A., "Preconditioning applied to variable and constant density flows," *AIAA Journal*, Vol. 33, No. 11, 1995, pp. 2050–2057.

[64]Goodwin, D. G., "An open-source, extensible software suite for CVD process simulation," *Chemical Vapor Deposition XVI and EUROCVD 14*, 2003, pp. 155–162.

[65]Law, C. K., "Comprehensive description of chemistry in combustion modeling," *Combustion Science and Technology*, Vol. 177, No. 5-6, 2005, pp. 845–870.

[66]Qin, Z., Lissianski, V. V., Yang, H., Gardiner, W. C., Davis, S. G., and Wang, H., "Combustion chemistry of propane: A case study of detailed reaction mechanism optimization," *Proceedings of the Combustion Institute*, Vol. 28, No. 2, 2000, pp. 1663–1669.

[67]Guo, H., Liu, F., Smallwood, G. J., and Gülder, Ö. L., "The flame preheating effect on numerical modelling of soot formation in a two-dimensional laminar ethylene-air diffusion flame," *Combustion Theory and Modelling*, Vol. 6, 2002, pp. 173–187.

[68]Honnery, D. R. and Kent, J. H., "Soot formation in long ethylene diffusion flames," *Combustion and Flame*, Vol. 82, No. 3-4, 1990, pp. 426–434.

[69]Kent, J. H. and Honnery, D. R., "Soot formation rates in diffusion flamesâĂŤa unifying trend," *Combustion Science and Technology*, Vol. 75, No. 4, 1991, pp. 167âĂŞ177.

[70]Bilger, R. W., "The structure of turbulent nonpremixed flames," *Proceedings of the Combustion Institute*, Vol. 22, No. 1, 1989, pp. 475–488.

[71]Megaridis, C. M., Griffin, D. W., and Konsur, B., "Soot-field structure in laminar soot-emitting microgravity nonpremixed flames," *Proceedings of the Combustion Institute*, Vol. 26, No. 1, 1996, pp. 1291–1299.

[72]Gülder, Ö. L., Thomson, K. A., and Snelling, D. R., "Effect of fuel nozzle material properties on soot formation and temperature field in coflow laminar diffusion flames," *Combustion and Flame*, Vol. 144, 2006, pp. 426–433.

[73]D'Anna, A. and Kent, J. H., "A model of particulate and species formation applied to laminar, nonpremixed flames for three aliphatic-hydrocarbon fuels," *Combustion and Flame*, Vol. 152, No. 4, 2008, pp. 573–587.

[74]Hall, R. J., Smooke, M. D., and Colket, M. B., "Prediction of soot dynamics in opposed jet diffusion flames," *Physical and Chemical Aspects of Combustion: A Tribute to Irvin Glassman*, edited by F. L. Dryer and R. F. Sawyer, Gordon & Breach, Amsterdam, 1997, pp. 189–230.

[75]Appel, J., Bockhorn, H., and Frenklach, M., "Kinetic modeling of soot formation with detailed chemistry and physics: Laminar premixed flames of C2 hydrocarbons," *Combustion and Flame*, Vol. 121, No. 1-2, 2000, pp. 122–136.